Geochemistry, Geophysics, Geosystems®

AGU ADVANCING EARTH AND SPACE SCIENCES

RESEARCH ARTICLE
10.1029/2025GC012719

Fault Stability Assessment in Tectonically Active Geothermal Fields Through Integrated Stress Analysis

Roberto Emanuele Rizzo[1,2], Derek Keir[2,3], Ameha Muluneh[4,5], Snorri Guðbrandsson[6], David Healy[7], Federico Sani[2], Giacomo Corti[8], and Paola Vannucchi[2]

[1]Department of Earth Sciences, Utrecht University, Utrecht, The Netherlands, [2]Department of Earth Sciences, University of Florence, Florence, Italy, [3]School of Ocean and Earth Science, University of Southampton, Southampton, UK, [4]MARUM Centre for Marine Environmental Sciences, University of Bremen, Bremen, Germany, [5]GFZ Helmholtz Centre for Geosciences, Potsdam, Germany, [6]ESMAP, The World Bank, Washington, DC, USA, [7]Geosolutions Leeds, School of Earth & Environment, University of Leeds, Leeds, UK, [8]Consiglio Nazionale delle Ricerche, Istituto di Geoscienze e Georisorse, Firenze, Italy

Key Points:

- Static fault stability analysis establishes critical baseline conditions for safe geothermal development
- The majority of faults in the Tulu Moye geothermal field are critically stressed under current stress conditions
- Small pore pressure increases of 3–5 MPa could reactivate critically stressed faults and trigger induced seismicity at reservoir depth

Supporting Information:

Supporting Information may be found in the online version of this article.

Correspondence to:

R. E. Rizzo,
r.e.rizzo@uu.nl

Citation:

Rizzo, R. E., Keir, D., Muluneh, A., Guðbrandsson, S., Healy, D., Sani, F., et al. (2026). Fault stability assessment in tectonically active geothermal fields through integrated stress analysis. *Geochemistry, Geophysics, Geosystems*, *27*, e2025GC012719. https://doi.org/10.1029/2025GC012719

Received 3 OCT 2025
Accepted 6 MAR 2026

Author Contributions:

Conceptualization: Roberto Emanuele Rizzo, Derek Keir, Paola Vannucchi
Data curation: Ameha Muluneh
Formal analysis: Roberto Emanuele Rizzo
Funding acquisition: Roberto Emanuele Rizzo, Derek Keir, Paola Vannucchi
Investigation: Roberto Emanuele Rizzo
Methodology: Roberto Emanuele Rizzo
Resources: Derek Keir, David Healy, Federico Sani, Giacomo Corti
Software: Roberto Emanuele Rizzo, Snorri Guðbrandsson

Abstract The Tulu Moye geothermal field in the actively deforming Main Ethiopian Rift presents substantial potential for renewable energy production, where interactions between fault systems, hydrothermal fluids, and tectonic activity require careful management for sustainable development. Here we present a first-order assessment of fault stability and reactivation risks under current stress conditions to establish baseline conditions for future geothermal operations. By combining stress inversion of earthquake focal mechanisms with structural mapping, we assess fault reactivation potential through slip tendency, dilation tendency, and fracture susceptibility analyses. We evaluate critical pore pressures and stress magnitudes required for rock failure using Monte Carlo simulations to quantify uncertainties in our geomechanical parameters. Our results indicate that several faults are critically stressed, with a modest pore pressure increase (3–5 MPa) potentially triggering fault slip and induced seismicity at 2 km depth. These findings align with observed microseismicity patterns linked to hydrothermal fluid flow, which enhances reservoir permeability but increases fault reactivation risks. Our static stress analysis provides an essential baseline framework for assessing fault stability and managing risks in geothermal systems in tectonically active regions.

Plain Language Summary Geothermal energy harnesses Earth's internal heat for renewable electricity generation. The Tulu Moye area in Ethiopia's Rift Valley shows strong geothermal potential, but developing these resources in tectonically active regions requires careful assessment of earthquake risks. Pumping fluids underground during geothermal operations may change subsurface pressures, potentially causing existing faults to slip and trigger earthquakes. We analyzed fault stability at Tulu Moye by examining natural earthquake patterns and mapping surface faults from satellite imagery. Computer simulations assessed how close these faults are to failure under current stress conditions. Our findings reveal that many faults are already critically stressed—rather like elastic bands stretched nearly to the breaking point. Even modest fluid pressure increases (roughly equivalent to adding 30–50 m of water column) could trigger fault slip and induce earthquakes. Significantly, pore fluid pressure emerged as the dominant control on fault stability, accounting for 45% of the uncertainty in our predictions. This baseline assessment identifies which faults pose the greatest risk and establishes safe operational thresholds. By understanding these constraints before development begins, operators can design appropriate monitoring systems and injection strategies to minimize seismic hazards whilst extracting geothermal resources.

1. Introduction

The reliance on traditional hydrocarbon resources must diminish as global efforts accelerate toward net zero carbon emission targets. Geothermal energy, as a renewable resource, has the potential to play a critical role in this energy transition (IEA, 2024). However, successful development of geothermal systems critically depends on understanding the reactivation potential of faults and fractures (Evans et al., 2012; Majer et al., 2007; Zang et al., 2014; Zoback, 2007). These geological features, despite comprising a small fraction of subsurface volume, can dramatically influence both the effectiveness and safety of geothermal operations through their control of fluid flow and mechanical stability (Kim et al., 2018).

Validation: Roberto Emanuele Rizzo
Visualization: Roberto Emanuele Rizzo
Writing – original draft: Roberto Emanuele Rizzo
Writing – review & editing: Roberto Emanuele Rizzo, Derek Keir, Ameha Muluneh, Snorri Guðbrandsson, David Healy, Federico Sani, Giacomo Corti, Paola Vannucchi

Successful geothermal reservoirs require intersection of permeable fractures and faults oriented favorably to the regional stress state (Kim et al., 2018). However, fault behavior can vary significantly: faults with high effective normal stresses may act as sealing barriers that compartmentalize reservoirs, while those under high dilatational stresses can create fluid leakage pathways during drilling. Such behavioral changes are further modulated by potential variations in the stress field itself (both in orientation and magnitude), which can shift over operational timescales in response to fluid withdrawal, injection, and thermal perturbations (Jeanne et al., 2014; Segall & Fitzgerald, 1998). This understanding is especially crucial in low-permeability formations where stimulation treatments become necessary. During reservoir stimulation, whether through hydrofracturing or hydro-shearing, flow path enhancement must be carefully managed (Liu et al., 2011; Moein et al., 2023). If fluid injection pressures are not properly adjusted to the prevailing stress conditions and rock frictional properties, they can reduce fault strength and trigger either aseismic or coseismic slip. Consequently, thorough characterization of the in situ stress tensor and its interaction with the fracture and fault network is essential before developing any deep geothermal system.

It is important to establish that comprehensive risk assessment for geothermal systems ultimately requires coupled thermo-hydro-mechanical-chemical (THMC) modeling to capture poroelastic, thermoelastic, and dynamic stress transfer effects (Raesenberg & Simpson, 1992); static fault—by which we mean static, deterministic baseline characterizations that do not account for transient or coupled thermo-hydro-mechanical effects—stability analysis provides essential baseline characterization. Such first-order assessments are necessary for: (a) initial well trajectory planning to optimize fracture intersection while avoiding critically stressed faults, (b) identifying structures requiring priority monitoring, and (c) establishing pre-production baseline conditions against which operational changes can be measured. This approach has proven valuable in numerous geothermal fields worldwide where static analyses informed initial development strategies before more complex modeling became feasible with production data (Evans et al., 2012; Kim et al., 2018).

These fundamental geomechanical considerations are particularly relevant given that geothermal energy production is well-documented for inducing geohazards, including earthquakes and ground subsidence, which threaten both operational sustainability and public safety (Kim et al., 2018; Moein et al., 2023). Even small perturbations in stress or fluid pressure—on the order of just a few megapascals—can significantly affect fault stability (Hincks et al., 2018; Moein et al., 2023; Raesenberg & Simpson, 1992; Stein, 1999). This sensitivity is dramatically illustrated by increased seismicity observed in Oklahoma and Texas following wastewater injection from hydraulic fracturing operations (Biggs et al., 2011; Hennings et al., 2021; Hicks et al., 2021). Several processes can promote fault reactivation in tectonically active geothermal provinces—reservoir pressure depletion, poroelastic stress changes and thermoelastic contraction (Hennings et al., 2021; Hicks et al., 2021). Here we restrict attention to the present-day stress state and static fault stability at Tulu Moye; coupled thermo-hydro-mechanical effects are outside our scope.

The Tulu Moye (TM) geothermal field in the actively deforming Main Ethiopian Rift exemplifies these challenges. Located approximately 100 km south of Addis Ababa, the field is set within a Quaternary to Recent volcanic complex characterized by calderas, resurgent volcanoes, and aligned cones (Biggs et al., 2011; Guðbrandsson et al., 2020; Kebede et al., 2023). Magnetotelluric surveys have identified key reservoir features, including a shallow clay cap approximately between 1 and 2 km depth and a magma reservoir below 4 km that serves as the heat source (Greenfield et al., 2019a, 2019b; Guðbrandsson et al., 2020). Seismic activity in the field, particularly shallow high-frequency microseismicity at 2–5 km depth, indicates active hydrothermal fluid migration with associated elevated pore pressures (Greenfield et al., 2019a, 2019b). Additionally, low-frequency earthquakes beneath the TM volcano provide evidence of high fluid pressures even below the hydrothermal circulation zone (Guðbrandsson et al., 2020).

Here we quantify the current state of stress in fault segments at reservoir depths (2 km below the surface) to better understand fault stability under geothermal operations at TM. We employ fault stability measures including slip tendency, dilation tendency, and fault susceptibility, and integrate these with probabilistic analyses using Monte Carlo simulations. Our analysis shows that many fault segments in the region are close to failure under the present stress regime, with even a modest increase in pore pressure potentially causing fault reactivation. This framework for characterizing the risk of fault slip aims to contribute to the development of sustainable and more efficient geothermal energy systems in tectonically active regions.

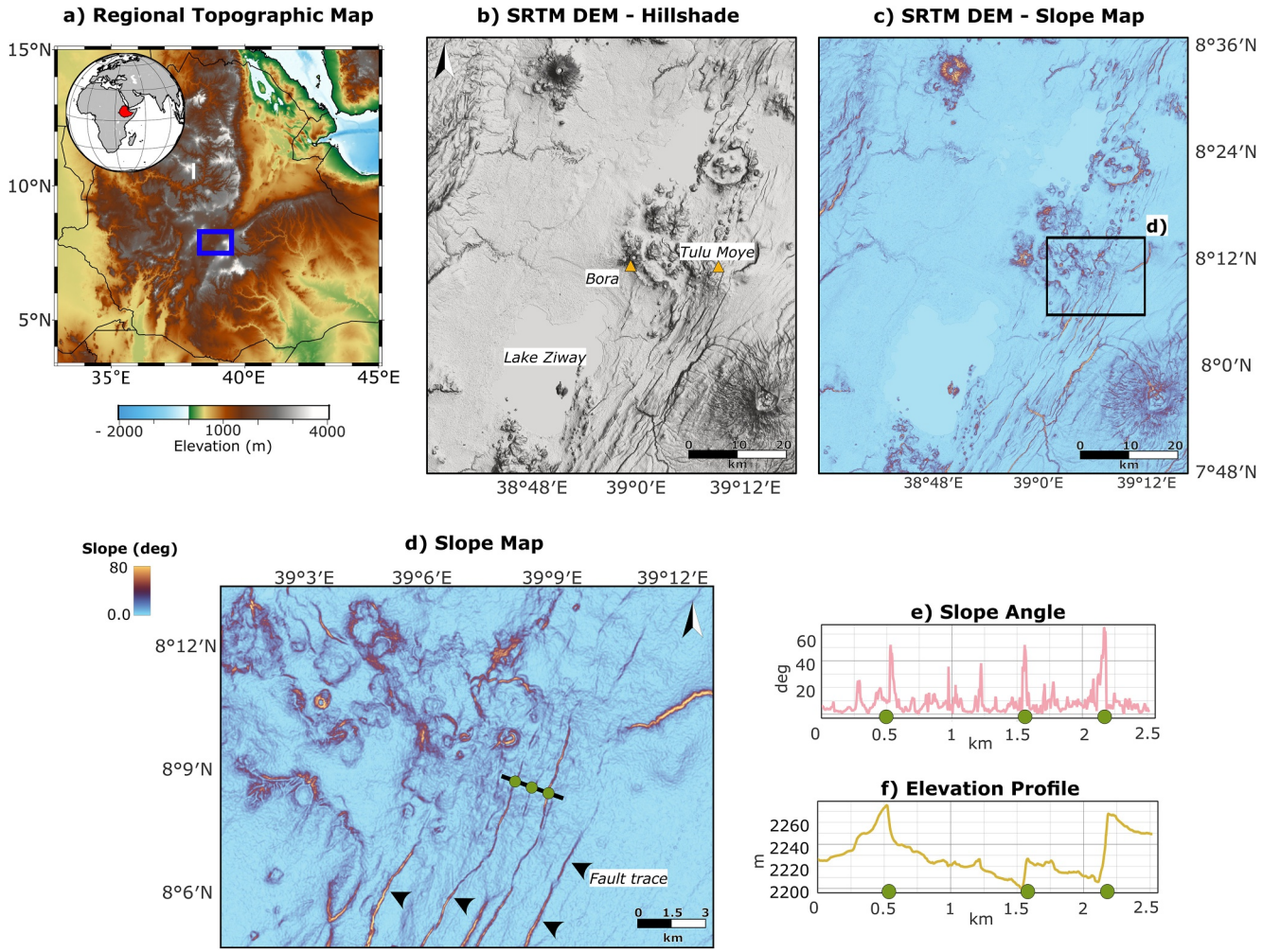

Figure 1. Location of the studied area and fault mapping method on the Digital Elevation Model (DEM). (a) Location of the Bora–Tulu Moye volcanic region (blue box) in relation to the Ethiopian Region. (b) SRTM DEM (Hillshade) of the rift with location of the main volcanic centers (Tulu Moye and Bora), and the location of Lake Ziway. (c) SRTM DEM Slope map of the rift; (d) Closer caption of the SRTM DEM Slope map in panel (c) high slope values (in bright colors) correspond to the steep fault scarps as confirmed by the Slope Angle in panel (e) and Elevation Profile plots in panel (f).

2. Methods

2.1. Fault Mapping

We utilized the 30 m (1 arc second) Shuttle Radar Topography Mission (SRTM) Global (JPL NASA, 2020; NASA, 2013) digital elevation model (DEM) to map faults in the Bora-Tulu Moye area (Figure 1a). The DEM has an absolute height error (90%) of 5.6 m in Africa (Rodriguez et al., 2006). Shuttle Radar data has been successfully used for remote fault mapping in the East African Rift (Laó-Davila et al., 2015; Wedmore et al., 2022), and offers global, freely accessible coverage. To identify faults, we applied the following criteria: (a) prominent, steep linear scarps (30–70°), particularly at the base of escarpments; (b) vertically offset, asymmetrical escarpments to differentiate them from fissures or river valleys (which typically form "V-shaped" troughs); and (c) persistent linear alignments. These criteria follow methods used by Agostini et al. (2011) and Corti et al. (2020), the latter of which focused on fault systems along the Asela-Langano Margin, located south of our study area.

We processed the DEM to derive *slope* and *hillshade* maps to minimize errors associated with fault mapping and improve visual interpretation (Figures 1b and 1c) Faults showing high slope angles (between 30° and 90°, as documented in Bonini et al. (1999) and Agostini et al. (2011)) were prioritized for mapping. The resulting fault lineaments were then analyzed using FracPaQ software (Healy et al., 2017) to extract fault attributes such as segment length, orientation, and length statistical distribution (Figure 2). The validity of extrapolating surface-

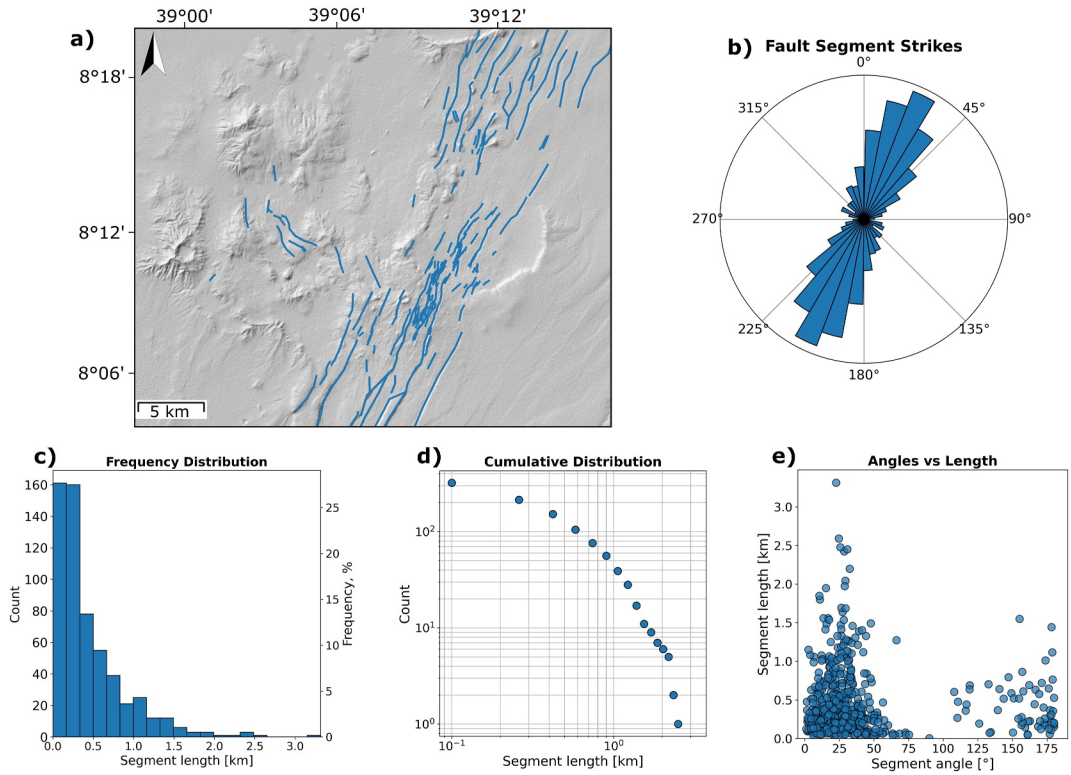

Figure 2. FracPaQ output of the fault mapped in the Bora—Tulu-Moye area. (a) Faults traced (blue lines) over the Digital Elevation Model (DEM). (b) Rose diagram showing the frequency of fault segment orientations (expressed as strike). (c) Histogram showing the fault segments length distribution. (d) Bi-logarithmic plot showing the cumulative frequency distribution of fault segments. (e) Plot showing the cross-correlation between fault segment orientations (strike) versus the segment lengths.

mapped structures to reservoir depths (~2–6 km) is supported by microseismic and gravity data. Earthquake swarms at ~2–6 km depth (depth below the surface) form several-kilometer-long clusters that align, in map view and in cross-section, with the surface fault traces (Figure 3), indicating structural continuity at depth (Greenfield et al., 2019b; Hochstein et al., 2017; Nigussie et al., 2023). Horizontal derivatives of the residual gravity field at Tulu Moye delineate NNE-striking lineaments beneath the rift-axis faults and NW–SE lineaments beneath the western caldera system, consistent with our mapped fault orientations (Hilemichaeil et al., 2024; Nigussie et al., 2023).

2.2. Stress State Determination and Analysis

The analytical model of the stress state was constructed using FracPaQ and follows the principles of effective stress analysis (Biot, 1941; Detournay & Cheng, 1993). The components influencing the effective stress include:

1. Overburden Stress (σ_V): The weight of the overlying rock as a function of depth and rock density. This vertical stress was calculated using $\sigma_V = \rho_R g h$, where ρ_R is the bulk density of the rock, g is the gravitational acceleration, and h is the depth. For geothermal reservoirs below TM, typical rock densities range from 2,500 to 2,800 kg/m^3 (Schwab et al., 2017; Zoback et al., 2003). The selected rock density values are consistent with published estimates for volcanic sequences and crystalline basement rocks (Schwab et al., 2017; Zoback et al., 2003) and represent a reasonable first approximation in the absence of borehole density logs or gravity-constrained density models for the TM field specifically.
2. Fluid Pressure (P_f): The fluid pressure within pores and cracks in the rock, influencing effective stress. Under hydrostatic conditions, P_f increases with depth at a rate of approximately 9.8 MPa/km (Fournier., 1991; Keir et al., 2006). However, in geothermal systems, fluid pressures can significantly deviate from hydrostatic pressure due to thermal effects and fluid circulation (Keir et al., 2006). Therefore, hydrostatic pore fluid pressure is adopted as the baseline condition, consistent with the absence of borehole pressure data at Tulu

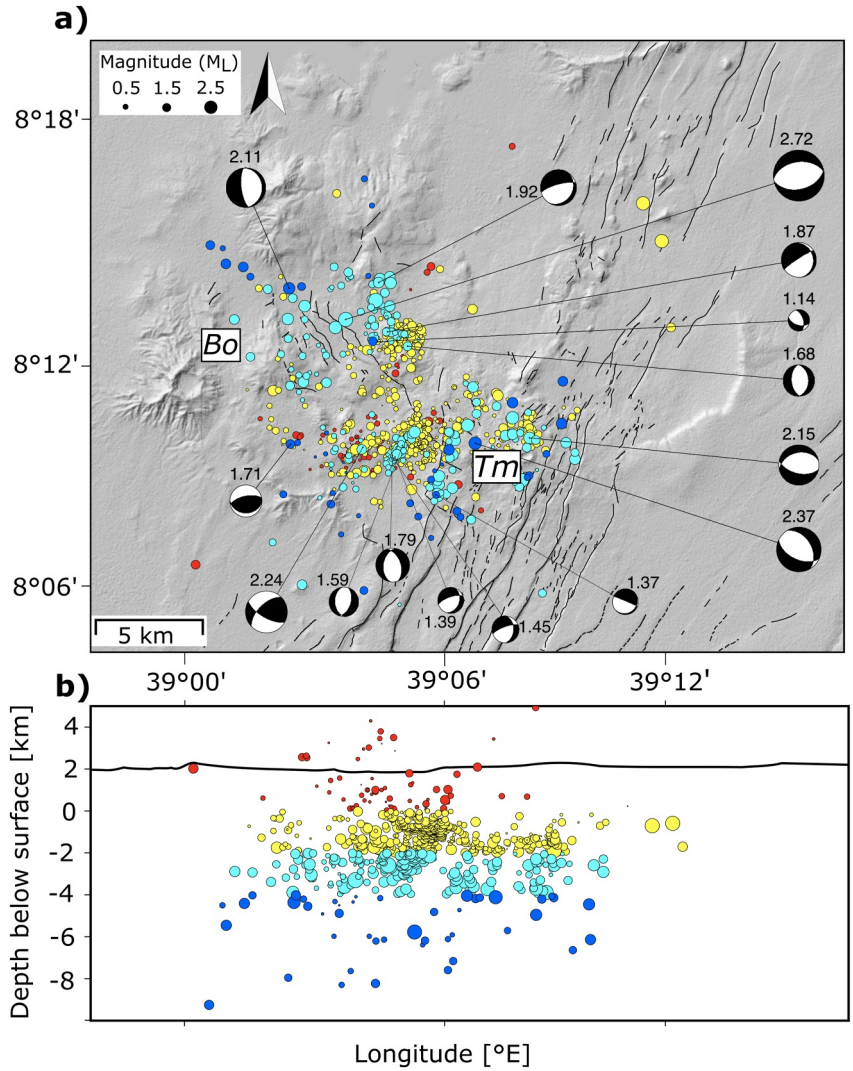

Figure 3. Seismicity and focal mechanisms in the Tulu-Moye area (after Greenfield et al., 2019a). (a) Map of detected earthquakes around the Bora (Bo)—Tulu Moye (Tm) volcanic complex. Earthquake hypocenters are indicated by the circles, scaled by calculated magnitude (<2.5 M_L), and colored by depth. The locations of earthquakes with well-constrained focal mechanisms are indicated by beach-balls (numbers next to the beach-balls show their magnitude). (b) Earthquakes hypocenters in a longitude versus depth cross section. The black line near the 2 km elevation is surface topography.

Moye and with conditions inferred for the shallow hydrothermal system from regional studies (Fournier, 1991; Keir et al., 2006).

3. Stress state: Including tectonic stresses and overburden stress. Effective stress calculations also account for the reduction in normal stress due to fluid pressure, defined by $\boldsymbol{\sigma_V = \sigma_V - P_f = (\rho_R - \rho_f)\, gh}$, where ρ_f is the fluid density. In extensional tectonic settings such as the Main Ethiopian Ridge (MER), the maximum principal stress (σ_1) is typically vertical, while the minimum principal stress (σ_3) is horizontal and perpendicular to the rift axis. The intermediate principal stress (σ_2) is typically horizontal and parallel to the rift axis (Keir et al., 2006; Muluneh et al., 2018).

The stress model accounts for depth-dependent variations in rock properties and considers the effects of structural heterogeneities. The model assumes the elastic behavior of the rock mass and isotropic pore pressure distribution at the scale of interest.

To complement the analytical stress model and better constrain the stress field orientation, we analyzed 15 well-determined earthquake focal mechanisms collected from a network of eight 3-component broadband

seismometers (Greenfield et al., 2019a, 2019b; Figure 3). We performed stress inversion analysis using the *STRESSINVERSE* Python software package (Vavryčuk, 2014), which incorporates Michael's method (Micheal, 1984, 1987) with an instability criterion proposed by Lund and Slunga (1999). While borehole stress measurements would provide higher spatial resolution, focal mechanism inversions remain the standard approach for stress characterization in rift systems where drilling data are unavailable. The consistency of focal mechanisms across our study area (standard deviation of P-axis orientations <15°) suggests that the regional and rift-wide stress field adequately represents reservoir-scale conditions, though we incorporate this uncertainty into our Monte Carlo analysis (Section 2.4).

Stress magnitudes were inferred based on extensional tectonic regimes typical of the MER, where: (a) σ_1 is the maximum principal stress (vertical), (b) σ_2 is the intermediate stress, and (c) σ_3 is the minimum principal stress (horizontal). The vertical stress ($\sigma_1 = \sigma_V$) was calculated using the depth and density of the overlying rock column, with $\sigma_V = \rho_R g h$. The minimum compressive stress (σ_3) was estimated using the frictional strength of optimally oriented faults:

$$\sigma_3 = \sigma_1 - \mu(\sigma_1 - P_f)$$

where μ is the static friction coefficient, set to 0.59 ± 0.16 based on the inversion of earthquake focal mechanisms for the whole northern MER, including the TM area (Muluneh et al., 2018). Given uncertainties in rock density (2,500–2,800 kg/m^3), stress magnitudes (±10%), and friction coefficient (0.59 ± 0.16), these parameters ranges were incorporated into our probabilistic analysis.

2.3. Slip Tendency, Dilation Tendency, and Fracture Susceptibility

The stress field and faulting processes in the Earth's crust are closely related phenomena. Faulting and fault reactivation are controlled by shear stress on the fault, pore-fluid pressure, cohesion and fault friction. In addition, the orientation of the fault with respect to the principal stress directions governs the susceptibility of the fault to be (re-)ruptured. An essential role in the assessment of risk of fault reactivation is played by the analysis of optimally oriented faults for shear failure (i.e., Mohr-Coulomb criterion) and thus being the most unstable under the given stress conditions. Once the in situ stress tensor is well understood, acting shear, τ, and effective normal (σ'_n; i.e., the normal stress minus the pore fluid pressure), stresses along any arbitrarily oriented planar feature can be resolved (Barton et al., 1995; Jaeger et al., 2007).

Various measures have been proposed to quantify the propensity or tendency of a given fault to slip (or open) in a known stress field. These methods are based on the assumption of Mohr-Coulomb (brittle-plastic) failure, which has been shown to capture the key aspects of faulting in the upper crust. We employed three complementary measures: slip tendency (T_s), dilation tendency (T_d), and fracture susceptibility (S_f).

A. Slip tendency (T_s) (Morris et al., 1996) is the ratio between shear stress (τ) and normal stress (σ_n). This ratio, which follows Amonton's law, is the simplest way to measure fault stability.

$$T_s = \frac{\tau}{\sigma_n - P_f} = \frac{\tau}{\sigma_h}$$

where τ is the shear stress and σ_h is the effective normal stress acting on the fault plane. These stress components depend on the principal stresses and the orientation of the fault plane [46]. Discontinuities with T_s approaching or exceeding the static coefficient of friction, μ, and absent cohesion (C_0) are assumed to have increased likelihood for a shear movement, Ts $\leq \mu$. This dimensionless index represents the fundamental mechanical principle of Mohr-Coulomb shear failure: as the shear stress increases relative to normal stress, the fault approaches failure.

Faults and fractures with increased likelihood for a shear movement can be simultaneously assumed to be hydraulically active (Barton et al., 1995; Morris et al., 1996). On the other hand, discontinuities with low T_s are considered to have low fluid flow potential and are expected to be "locked" in the in situ stress state (Lisle & Srivastava, 2004).

B. Dilation tendency (T_d) describes the propensity for a fault to open in a given stress regime:

$$T_d = \frac{\sigma_1 - \sigma'_n}{\sigma_1 - \sigma_3}$$

where σ_1 and σ_3 are the effective principal stresses (i.e., the principal stresses minus the pore fluid pressure) of the in situ stress tensor (Ferrill et al., 2020) High T_d values indicate greater potential for fluid flow and permeability along the fault plane.

C. Since most rocks in the upper crust, including fault rocks, are porous and typically fluid-saturated, we must consider pore fluid pressure and effective stress in assessing fault stability. *Fault susceptibility* (S_f)—also known as critical pore pressure (ΔP_f)—quantifies the change in pore fluid pressure needed to push a stressed fault to failure (Healy & Hicks, 2022; Streit & Hillis, 2004). Fluid-driven shear reactivation is dependent on the shear and normal stresses acting on the plane, as well as its cohesion (here assumed = 0), and static coefficient of friction (μ):

$$S_f = \Delta P_f = \sigma_h - \frac{\tau - C_0}{\mu}$$

where P_f is the pore fluid pressure at the fault, μ is the static friction coefficient, and C_0 is the cohesion. Reactivation via fluid-driven dilation would require a fluid pressure greater than the fracture susceptibility.

The computed values of T_s, T_d, S_f for mapped fault segments are derived from the distributions of several input parameters, including the magnitudes of vertical (V_σ), minimum horizontal ($\sigma_{h\ \mathrm{min}}$), and maximum horizontal ($\sigma_{H\ \mathrm{max}}$) stresses, the azimuth of $\sigma_{H\ \mathrm{max}}$, and P_f. For an extensional tectonic regime like the MER, σ_V corresponds to σ_1, $\sigma_{H\ \mathrm{max}}$ to σ_2, and $\sigma_{h\ \mathrm{min}}$ to σ_3. All fault segment planes are modelled as cohesionless surfaces and assigned the appropriate static coefficient of friction (μ) for reactivation (i.e., 0.59 ± 0.16; Muluneh et al., 2018).

2.4. Probabilistic Modeling: Monte Carlo Simulations and Response Surface Methodology

To account for uncertainties in stress, pore pressure, and fault properties, we applied Monte Carlo simulations combined with Response Surface Methodology (RSM) (Healy & Hicks, 2022). To assess fault stability probabilistically, this approach provides a parametric representation of the relationship between fault stability metrics (e.g., slip tendency, dilation tendency, and fracture susceptibility) and input variables such as stress magnitudes, fault orientations, and friction coefficients. Healy and Hicks (2022) RSM use a *3q* factorial design, where input variables span their respective parameter spaces through predefined sampling points. Then, a quadratic polynomial function approximates the response, allowing interaction and nonlinear effects. Finally, the polynomial coefficients were determined using least squares regression. The response surface is then integrated with Monte Carlo simulations to evaluate the cumulative distribution of fault stability metrics. Input variables were randomly sampled from their respective probability distributions (normal, skewed normal, or von Mises), reflecting realistic uncertainties in (a) Stress magnitudes and orientations; (b) Pore pressures; and (c) Fault geometries and properties. Monte Carlo simulations generate a range of possible outcomes based on these input variable distributions. Thus, Monte Carlo sampling is used to propagate parameter uncertainties through the fracture susceptibility calculation: input parameters (stress magnitudes, pore fluid pressure, cohesion, and friction coefficient) are drawn from their respective probability distributions and fracture susceptibility is recomputed for each sample, rather than simulating forward physical processes.

The RSM fitted quadratic surfaces to the simulation outputs, enabling us to predict slip and dilation probabilities across the Tulu Moye area. Sensitivity analyses identified the most influential parameters affecting fault behavior. This combined RSM-Monte Carlo approach provides a robust framework for (a) Quantifying uncertainties in geomechanical modeling; (b) Understanding the conditions under which fault reactivation might occur; and (c) Managing risks associated with geothermal operations.

Table 1
Orientation of the Three Principal Stresses as Derived From the Stress Inversion

	Azimuth	Plunge
σ_1	204.2	81.3
σ_2	356.3	7.6
σ_3	86.8	4.0

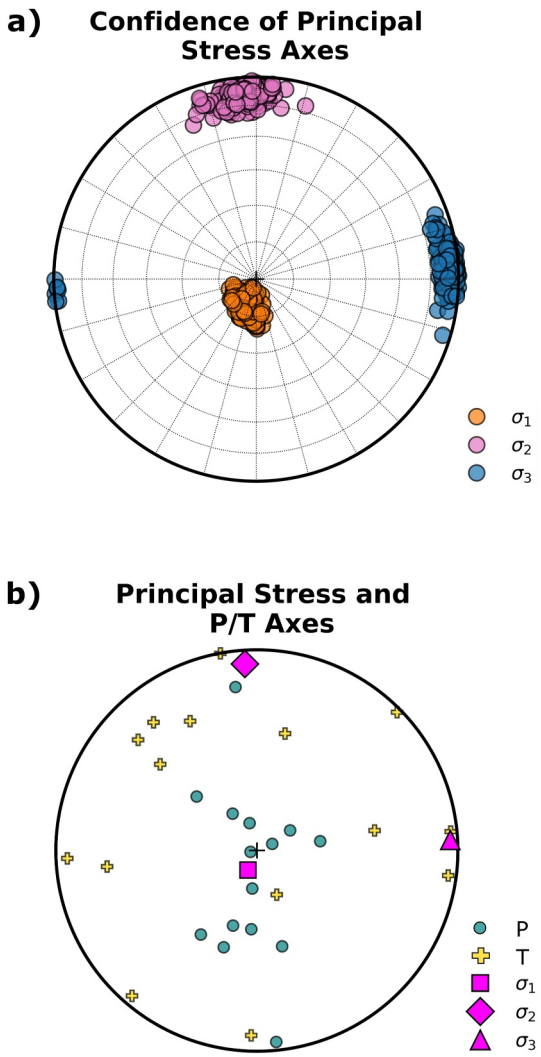

Figure 4. Confidence limits of the principal stress directions (a) as resulted from the focal mechanisms (values are reported in Table 1). P/T axes with retrieved principal stress directions (b). The P and T axes are marked by teal circles and yellow plus signs, respectively.

3. Results

3.1. Stress Inversion and Stress Orientation

The inversion revealed the orientations of the principal stresses. The results indicate a maximum principal stress (σ_1) oriented at an azimuth of 204.2° and a steep plunge of 81.3°. The intermediate principal stress (σ_2) shows an azimuth of 356.3° with a shallow plunge of 7.6°. The minimum principal stress (σ_3) is oriented horizontally at an azimuth of 86.8° and a plunge of 4.0° (Table 1 and Figure 4). These orientations are compatible with an extensional stress regime typical of the Main Ethiopian Rift (Hutchison et al., 2015).

From the inversion of the focal mechanisms, we also calculated the stress ratio

$$R = \frac{\sigma_1 - \sigma_2}{\sigma_1 - \sigma_3}$$

which represents the difference between the three principal stresses. The optimum shape ratio determined from the distribution of the P and T axes on the focal sphere was 0.67. The confidence limits of the principal stress axes, obtained by perturbing the focal mechanism data set, are shown in Figure 4. The *STRESSINVERSE* code calculated two conjugate focal mechanisms (principal focal mechanisms) compatible with the principal stress axes, both representative of normal faulting.

To assess the robustness of the shape ratio R and stress tensor orientation to the choice of uncertainty estimation method, we additionally applied the ILSI package (Beaucé et al., 2022), which implements the Vavryčuk (2014) iterative inversion with bootstrapped resampling. The ILSI analysis yields $R = 0.74$–0.81 depending on the inversion variant, with 95% confidence intervals spanning approximately 0.16–0.97. These results are consistent with the STRESSINVERSE solution within uncertainty, and the wide confidence intervals reflect the limited size of the focal mechanism data set ($n = 15$) and the presence of trans-tensional mechanisms within it (Figure 3). The stress orientations recovered by both methods are in good agreement (σ_1 plunge > 74°, σ_3 near-horizontal at ~77°–88° azimuth), and the principal stress directions used in the fault stability analysis are therefore considered robust. Full bootstrapped results are presented in Figure S4 and Table S1 of Supporting Information S1.

The magnitudes of the principal stresses were calculated for two key seismic depth intervals identified in the TM field (Table 2). At 2 km depth, corresponding to shallow seismicity, σ_1 reaches 55 MPa, σ_2 is 40 MPa, and σ_3 is 33 MPa, with a pore fluid pressure (P_f) of 20 MPa. At 6 km depth, where deeper seismicity is observed (Greenfield et al., 2019a, 2019b), the principal stresses increase to $\sigma_1 = 165$ MPa, $\sigma_2 = 120$ MPa, and $\sigma_3 = 101$ MPa, with P_f reaching 59 MPa. These values reflect the depth-dependent increase in lithostatic load and follow the expected stress gradients for an extensional tectonic regime.

3.2. Slip and Dilation Tendency

To assess the potential for fault reactivation, we calculated the slip tendency (T_s) and dilation tendency (T_d) at 2 km depth, which represents the base of the clay cap and top of the main geothermal reservoir as identified by magnetotelluric surveys (Hutchison et al., 2015; Samrock et al., 2018). This depth

Table 2
Magnitude of the Three Principal Stresses Derived for the Two Seismic Depth Intervals: 2 km—Shallow Seismicity, and 6 km for the Deep Seismicity Zone (Greenfield et al., 2019a, 2019b)

2 km depth	6 km depth
σ_1 = 55 MPa	σ_1 = 165 MPa
σ_2 = 40 MPa	σ_2 = 120 MPa
σ_3 = 33 MPa	σ_3 = 101 MPa
P_f = 20 MPa	P_f = 59 MPa

corresponds to the transition from the low-resistivity clay seal to the underlying hydrothermal system and coincides with the shallow seismicity cluster (Greenfield et al., 2019a, 2019b). For a comprehensive overview, slip and dilation tendency for the mapped fault data are visualized as (a) color-coded line traces over the DEM, (b) contoured pole-to-plane over a lower hemisphere stereographic projection, and (c) three-dimensional (3D) Mohr representations (shear vs. effective normal stress normalized by the vertical stress).

Our results indicate that many faults in the TM area show high slip tendency values, particularly those aligned with the prevailing stress field (Figure 5). These faults are therefore more susceptible to slip under existing stress conditions.

We also evaluated the dilation tendency (T_d), which measures the potential for faults to dilate or open under the current stress regime. Dilation tendency is critical for understanding fluid flow, as faults with high T_d values may enhance permeability. Our analysis shows that faults in the Tulu Moye area, particularly at 2 km depth, exhibit moderate dilation tendencies (Figure 6), suggesting potential zones of enhanced fluid mobility within the geothermal system.

The spatial distribution of slip and dilation tendencies shows a strong correlation with fault orientation. NW-SE and NE-SW oriented structures exhibit the highest slip tendency (Figure 5a), reflecting their optimal orientation relative to the extensional stress regime characteristic of the MER (Agostini et al., 2011). In contrast, N-S oriented structures show the lowest slip tendency but the highest dilation tendency (Figure 6a), while E-W oriented faults display the lowest dilation tendency. This orthogonal relationship between slip and dilation tendencies reflects the orientation of principal stresses in the area, where σ_3 is oriented approximately E-W (86.8°). These orientation-

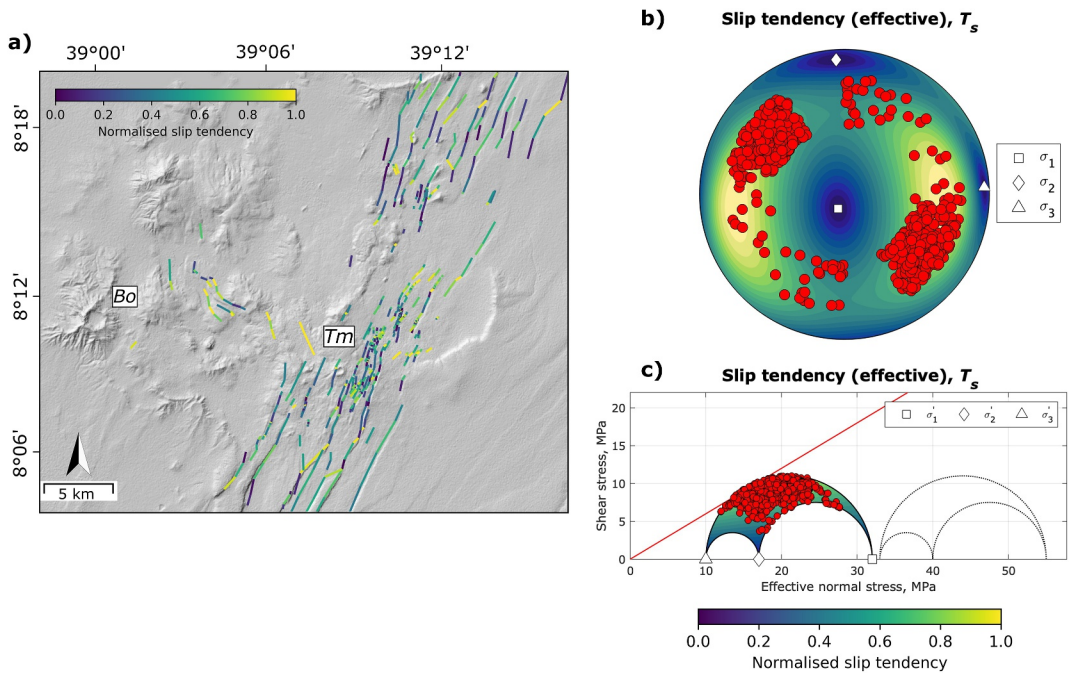

Figure 5. Results of the slip tendency analysis modeled at 2 km depth. (a) Map of the fault segments color-coded based on their likelihood to shear: darker colors indicate discontinuities with low slip tendency, while light-colored traces show those faults approaching or exceeding frictional resistance for sliding. (b) Lower hemisphere stereographic projection of (effective) T_s, showing contoured pole-to-plane values (red circles) for the mapped fault segments. The white square, diamond and triangle indicate the orientation of the three principal stresses—σ_1, σ_2, σ_3 respectively—as derived from stress inversion (Figure 4). (c) Fault data (red circles) in three-dimensional (3D) Mohr representations contoured for values of normalized slip tendency ($0 < T_s < 1$); the dotted 3D Mohr circle shows the stress state without the contribution of the hydrostatic pore fluid pressure.

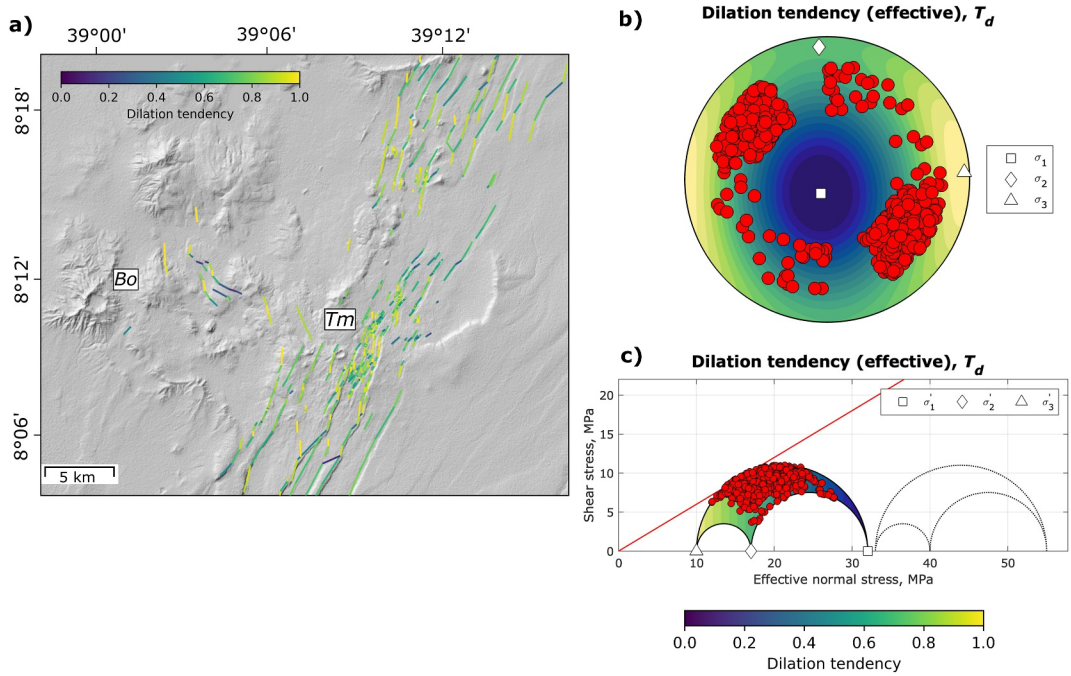

Figure 6. Results of the dilation tendency analysis modeled at 2 km depth. (a) Map of the fault segments color-coded based on their likelihood to dilate: darker colors indicate discontinuities with low dilation tendency, while light-colored traces show faults with high dilation tendency. (b) Lower hemisphere stereographic projection of (effective) T_d, showing contoured pole-to-plane values (red circles) for the mapped fault segments. The white square, diamond and triangle indicate the orientation of the three principal stresses $\sigma1$, $\sigma2$, $\sigma3$ respectively, as derived from stress inversion (Figure 4). (c) Fault data (red circles) in three-dimensional (3D) Mohr representations contoured for values of normalized dilation tendency ($0 < T_d < 1$); the dotted 3D Mohr circle shows the stress state without the contribution of the hydrostatic pore fluid pressure.

dependent mechanical behaviors have important implications for both fluid pathways and the likelihood of fault reactivation during geothermal operations.

Analysis of slip tendency and dilation tendency indicates that the most stable fault planes (normalized tendency of about 0) have their normals close to σ_2 or σ_3. The most unstable fault planes (with tendency close to 1) have their normals in directions between σ_1 and σ_3, being inclined from σ_3 by about 32° for a fault friction of 0.59 ± 0.16 (Muluneh et al., 2018). This orientation relationship between fault planes and principal stresses provides a framework for identifying critically stressed faults in the geothermal systems. The partial overlap between regions of high T_s and high T_d (Figures 5 and 6) suggests that fractures dipping at a low angle to the σ_1–σ_3 plane could be reactivated as mixed-mode (hybrid) fractures.

3.3. Fault Susceptibility and Critically Stressed Faults

Fracture susceptibility (S_f) measures the increase in pore fluid pressure required to induce fault reactivation. By projecting fault planes into Mohr space, we estimate the critical pore fluid pressure that promotes failure. Using the calculated stress state at 2 km depth, we estimated the fracture susceptibility for the mapped faults. The results show that a relatively small increase in pore pressure (≤5 MPa) could push several faults to the point of failure, particularly those already critically stressed (Figure 7).

We modeled the critically stressed faults at 2 km depth under varying pore pressure conditions. Optimally oriented faults would require an additional pore fluid pressure of 3 MPa—from the initial hydrostatic conditions (20 MPa)—to induce favorable conditions for failure on several fault segments (red lines and red petals of the associated rose diagram; Figure 8). A 5 MPa increase in pore pressure, instead, brings additional fault segments into a critically stressed state (Figure 8). These results suggest that even modest fluctuations in pore pressure, associated with geothermal operations, could trigger fault slip and potentially induce seismicity in the Tulu Moye area.

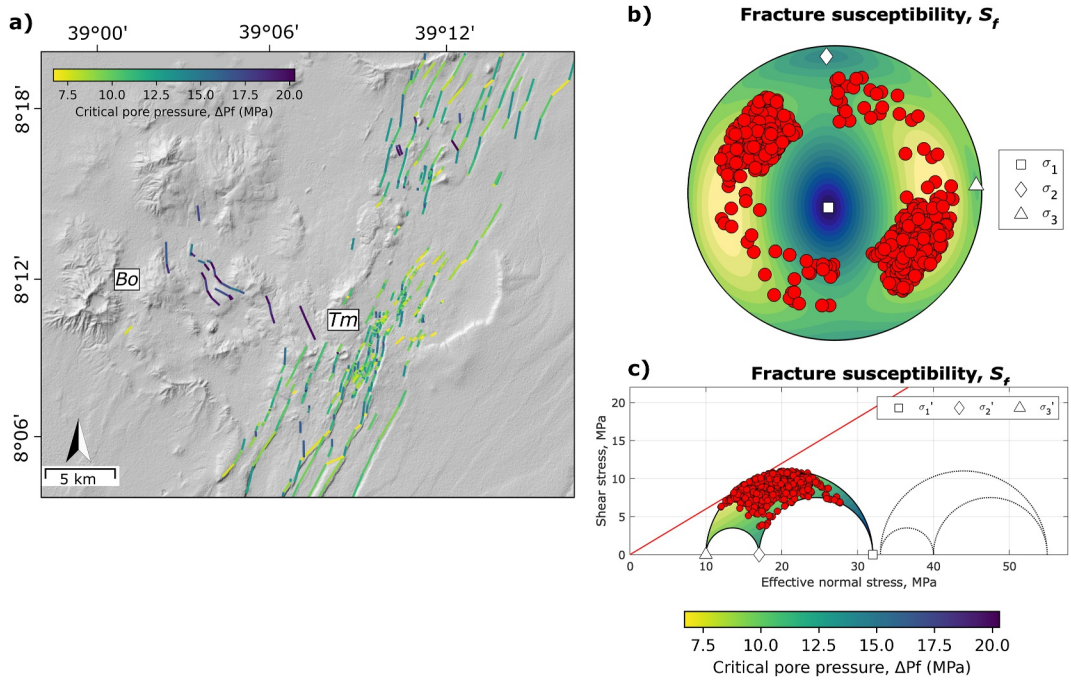

Figure 7. Results of the fault susceptibility analysis modeled at 2 km depth. (a) Map of the fault segments color-code based on the critical pore pressure ΔP_f (i.e., magnitude of fluid pressure change) required to cause shear reactivation: darker colors indicate discontinuities with high ΔP_f, while light-colored traces show faults with low ΔP_f. (b) Lower hemisphere stereographic projection of S_f, showing contoured pole-to-plane values (red circles) for the mapped fault segments. The white square, diamond and triangle indicate the orientation of the three principal stresses σ_1, σ_2, σ_3 respectively, as derived from stress inversion (Figure 4). (c) Fault data (red circles) in three-dimensional (3D) Mohr representations contoured for values of fault susceptibility (ΔP_f in MPa); the dotted 3D Mohr circle shows the stress state without the contribution of the hydrostatic pore fluid pressure.

3.4. Monte Carlo Simulation and Sensitivity Analysis

Given the uncertainties in the mechanical parameters, as identified in Section 2.4, we conducted Monte Carlo simulations (10,000 iterations) to assess the variability in the parameter used to model reactivation across the fault population. Figure 9a shows the distribution of the input parameters used in the Monte Carlo analysis of Fracture Susceptibility ($\boldsymbol{S_f}$). Each histogram (blue) represents the range and distribution of values calculated for vertical stress (i.e., σ_1), maximum and minimum horizontal stresses (i.e., σ_2,$\boldsymbol{\sigma_3}$ respectively), friction coefficient, cohesion, and pore fluid pressure ($\boldsymbol{P_f}$). The dark blue dashed lines indicate the values derived from our analysis: stress magnitudes from Table 2 (σ_1 = 55 MPa, σ_2 = 40 MPa, σ_3 = 33 MPa, and $\boldsymbol{P_f}$ = 20 at 2 km depth) and friction coefficient ($\boldsymbol{\mu = 0.59 \pm 0.16}$) from Muluneh et al. (2018). The distributions around these values reflect both natural variability in the fault population and measurement uncertainties.

We calculated a quadratic response surface and used a Monte Carlo simulation (N_{MC} = 10,000) to generate the ensemble summarized in Figure 9. The mode of the distribution of $\boldsymbol{S_f}$ is 2.9 MPa, meaning that, on average, an increase in pore fluid pressure of about 3 MPa above the average in situ value of 20 MPa is needed to push the effective stress state to Mohr–Coulomb failure. The histogram in Figure 9b is bimodal, with a clear skewness to lower values, and this is reflected in the CDF plot (Figure 9b). The distribution is overwhelmingly constrained between 0 and 20 MPa, meaning that the studied fault systems are likely unstable for any change in pore fluid pressure at these conditions. The response surface sections for $\boldsymbol{\mu}$, $\boldsymbol{C_0}$, and $\boldsymbol{P_f}$ shown in Figure 9a (red dots) all show a strong influence on the fracture susceptibility, and these are confirmed in the tornado plot of Figure 9c. Pore fluid pressure exhibits a negative correlation with $\boldsymbol{S_f}$ (Figure 9a), which is consistent with the general principle of effective stress: that is, if the original in situ pore pressure is already high, it only takes a small perturbation (small $\boldsymbol{P_f = S_f}$) to promote sliding failure. The sensitivity analysis, visualized as tornado plot (Figure 9c), reveals the relative influence of different input parameters on fault stability predictions. Each horizontal bar represents the percentage contribution to the total variance in fault reactivation probability when that parameter is varied across

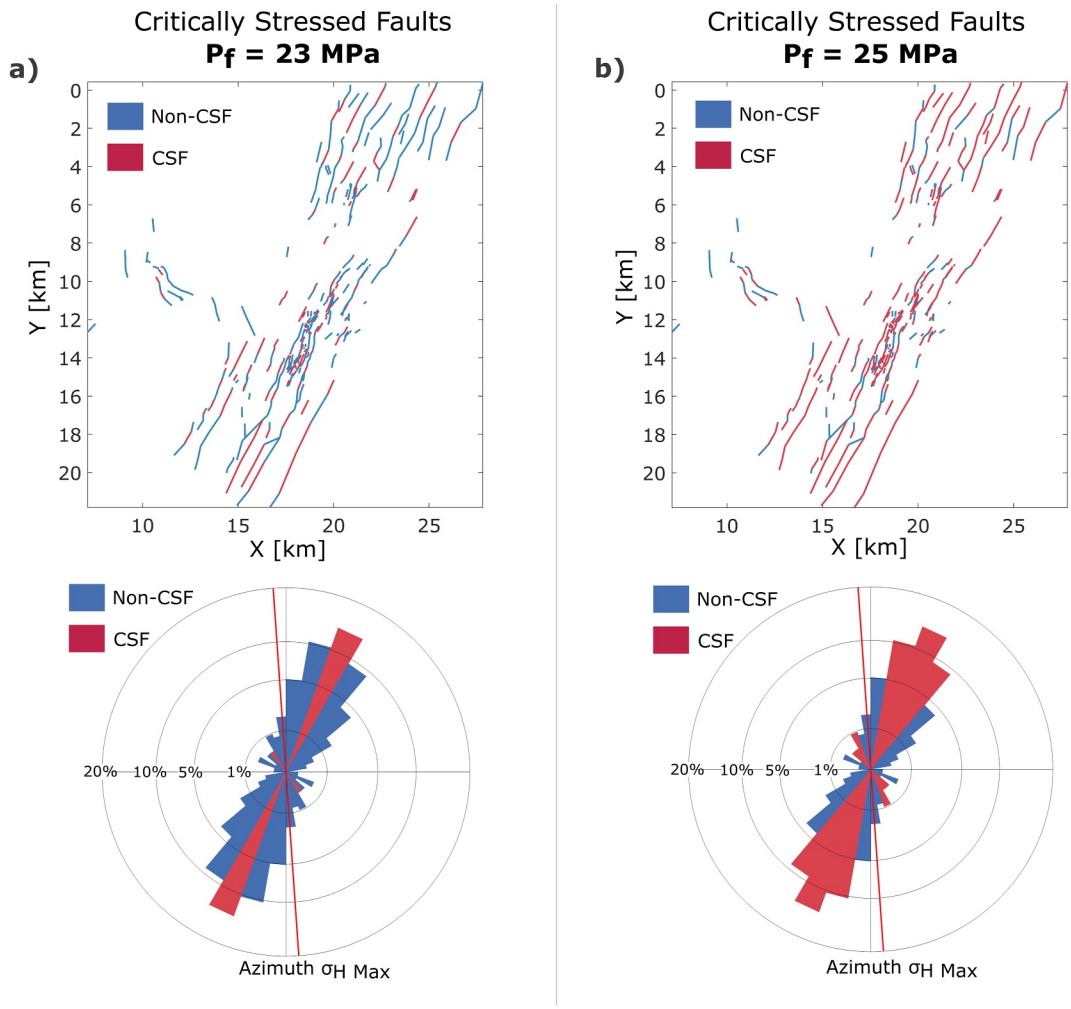

Figure 8. Modeled critically stressed faults (CSF) as deviation from the current hydrostatic condition. We modeled two possible scenarios of pore fluid increase: (a) a relatively small increase of pore fluid pressure, that is, 3 MPa from the current hydrostatic pressure condition (P_f = 20 MPa at 2 km depth). (b) Marked increase in pore fluid pressure (5 MPa). The two top figures illustrate fault segment traces for the critically stressed faults (red lines), while the bottom figures show the relative rose diagrams (red petals indicate the strikes for the critically stressed faults).

its uncertainty range while holding others constant. Pore fluid pressure emerged as the most significant variable, accounting for 45% of the variation in stability predictions. The magnitude of σ_1 is the second most influential parameter (30% of variation), followed by fault orientation (15%). Cohesion and friction coefficient showed lower sensitivity, together accounting for less than 10% of the variability in the model outputs (Figure 9c).

4. Discussion

4.1. Fault System Architecture and Seismic Response

The TM field's fault system exhibits complex behavior, with multiple fault segments of varying orientations that intersect and activate at different times and depths (Greenfield et al., 2019a, 2019b). The orientation of principal stresses, independently confirmed through focal mechanism inversion and foci clustering, controls fault behavior. Analysis of mapped fault segments using Mohr-Coulomb failure criteria reveals that most of the fault segments exhibit high slip tendency (>0.6), indicating optimal orientation for shear failure under the current stress regime. However, some fault segments show unfavorable orientations relative to the principal stress field, as evidenced by their position in the lower part of the 3D Mohr Circles.

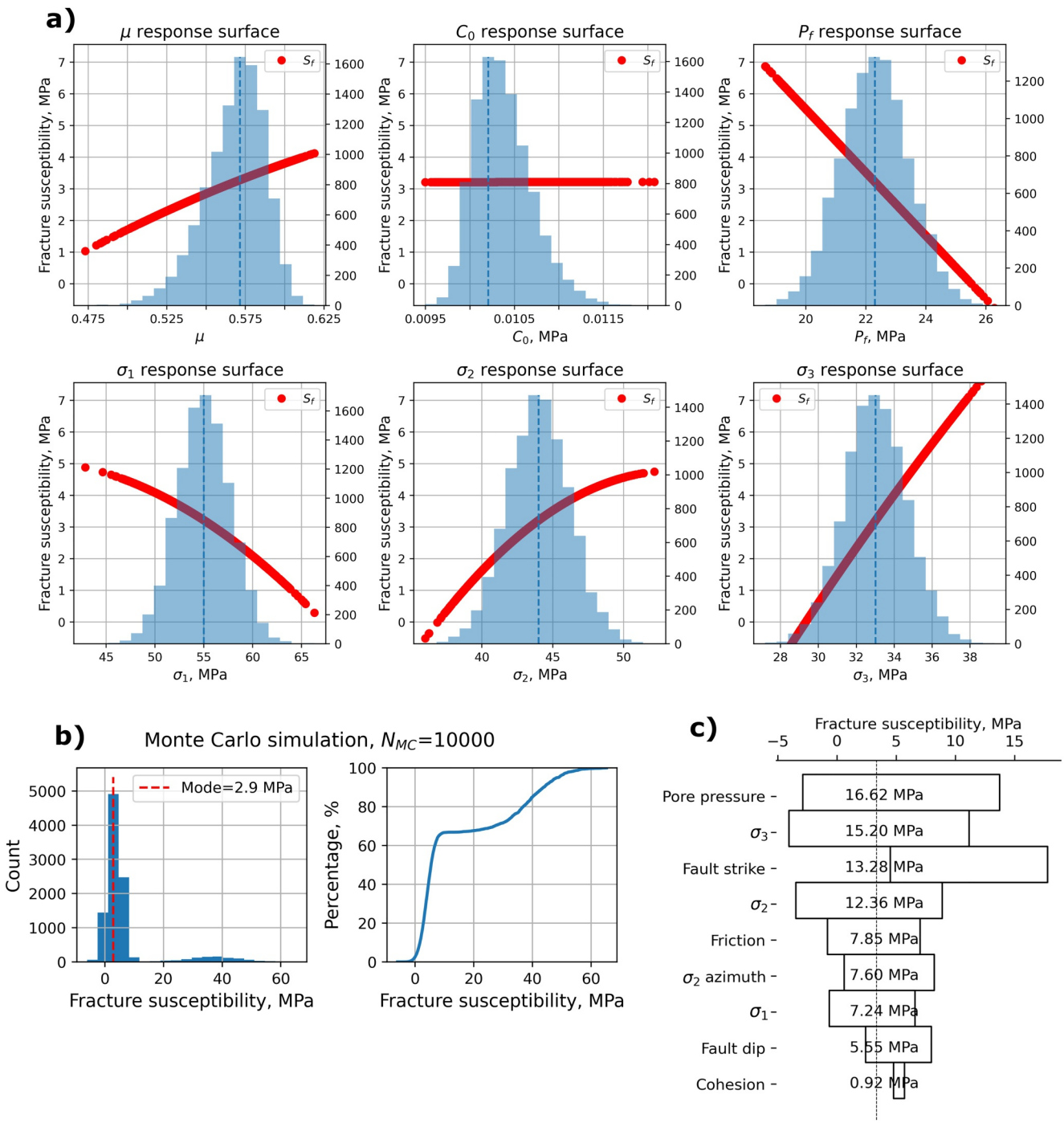

Figure 9. Monte Carlo simulation for fault reactivation analysis at 2 km depth. (a) Histograms of the input variables (blue histogram), used to calculate fracture susceptibility (S_f—red dots): stress magnitudes from depth calculations (Table 2), stress orientations from focal mechanism inversion (Table 1), and friction coefficient from regional studies (Muleneh et al., 2018). Note the skewed (asymmetric) distributions for static friction coefficient (μ) and Cohesion (C_0). (b) Output from Monte Carlo simulations (N_{MC} = 10,000) of fracture susceptibility (S_f) calculated using a quadratic response surface from synthetic input data in worked example two. Left: Histogram of calculated S_f, showing a bimodal distribution with a mode of 2.9 MPa. Right: Cumulative distribution function (CDF) of calculated fracture susceptibility, showing the range in values from just less than 0 to about 60 MPa. (c) Tornado plot showing sensitivity analysis: horizontal bars represent the percentage contribution to variance in fracture susceptibility (critical pore pressure) for each parameter.

These critically oriented faults can serve as pathways for both vertical and lateral fluid migration, potentially linking deeper magmatic systems to the shallower hydrothermal system. The role of these faults in fluid transport is particularly evident in transverse structures, especially those associated with caldera rims, which facilitate both vertical and lateral fluid migration (Greenfield et al., 2019a, 2019b; Kebede et al., 2023).

Fault reactivation at the TM could be exacerbated by geothermal activities. The injection and withdrawal of fluids during geothermal operations can alter subsurface pore pressures and stresses, potentially destabilizing existing faults. Therefore, a comprehensive understanding of the interplay between geothermal operations and fault systems is crucial to mitigate potential hazards and ensure the safe and sustainable development of geothermal energy at TM.

Our analysis shows that several faults in the area are already critically stressed, and even small increases in pore pressure could trigger fault slip. This finding aligns with Muluneh et al. (2018), who demonstrated that faults in the Main Ethiopian Rift are favorably oriented for reactivation under the current stress regime. Fluid injection, commonly used in geothermal operations, can significantly increase the pore pressure, reducing the effective normal stress on faults and promoting slip. Our Monte Carlo simulations further support this, showing that pore pressure is the most sensitive parameter influencing fault reactivation.

The complex interplay between tectonic setting, fault geometry, and geothermal operations at TM presents both opportunities and challenges for sustainable reservoir management. Our analysis reveals that the combination of pre-existing fault networks, active hydrothermal fluid flow, and the potential for pore pressure perturbations requires careful planning of injection strategies. The temporal and spatial patterns of seismicity reflect the evolution of the stress field during geothermal operations, with mechanical properties of faults playing a crucial role in determining whether slip occurs seismically or aseismically.

4.2. Implications for Geothermal Operations

The Tulu Moye geothermal project's developmental challenges arise from its fault-controlled nature. Due to the scarce intrinsic matrix porosity and permeability of the formation rocks in the TM region (Muluneh et al., 2018), future geothermal systems will rely primarily on faults and fracture networks. Well planning strategies should optimize the use of hydraulically active discontinuities, with drilling in the E–W or ESE–WNW directions being most advantageous for reservoir secondary permeability. However, when intersecting major NE-SW or secondary WNW-ESE-striking normal faults, seismic activity becomes likely, particularly during hydraulic stimulation. To mitigate this risk, fault segments with a lower slip tendency should be targeted for drilling operations.

This approach can be generally extended to the Central MER region, where most geothermal prospects are structurally controlled by regional fault systems. For instance, at the nearby Aluto Langano geothermal field, the NNE-SSW trending Wonji Fault Belt and parallel Artu Jawe Fault Zone act as major conduits for geothermal fluid flow (Hochstein et al., 2017). However, varying local stress conditions and structural complexities necessitate individual probabilistic risk and hazard analyses for each geothermal development in the region, particularly given that natural seismicity in the area already reaches magnitudes up to M_L 4.0 (Greenfield et al., 2019a), with larger events possible along major rift border faults.

Sustainable geothermal resource management requires careful consideration of pressure changes induced by fluid extraction and reinjection. Our results indicate that even modest pore pressure changes of 3–5 MPa could trigger fault reactivation. This sensitivity necessitates careful management of fluid injection rates and continuous monitoring of seismic activity. Experience from geothermal fields in tectonically active regions demonstrates the importance of adaptive management strategies. The Hellisheiði field in Iceland modified injection strategies after experiencing induced events, successfully reducing seismicity while maintaining production (Juncu et al., 2020). Similarly, high-temperature fields in New Zealand have developed operational protocols that accommodate both natural tectonic seismicity and injection-related events (Hopp et al., 2019).

The interaction between magmatic, tectonic, and hydrothermal processes complicates fluid extraction operations. Prolonged geothermal exploitation can alter the stress state of fault systems in spatially heterogeneous ways, as injection and production activities vary in both location and intensity over time. These variations can trigger fault slip or dilation, increasing the likelihood of induced seismic events.

A robust monitoring strategy is essential for safe operations. This should integrate real-time seismic monitoring, continuous pore pressure measurements, and regular assessment of stress state changes (Lee et al., 2019). Additionally, temperature variations must be tracked to understand thermal effects on the reservoir system. These monitoring data can be integrated with our probabilistic framework to provide ongoing assessment of fault stability conditions during production.

A primary mechanism for induced seismicity is stress change due to fluid operations: decreasing pore fluid pressure (P_f) during production increases the effective normal stress on faults, inhibiting fault slip, while injection operations can have the opposite effect by increasing it (Guo et al., 2023; Zbinden et al., 2020). Studies at the San Emidio geothermal field showed that production can actually enhance fault stability by reducing pore pressure and increasing effective normal stress on fault surfaces (Guo et al., 2023). This principle could be applied at Tulu Moye by preferentially producing from critically stressed zones while targeting injection toward more stable fault segments, though careful consideration of the reservoir's hydraulic connectivity would be essential (Guo et al., 2023; Kivi et al., 2022).

Successfully managing the TM geothermal system requires adaptive operational strategies that respond to monitoring data. This includes careful selection of injection sites to avoid critically stressed faults and development of pressure thresholds based on our stability analysis. Operational decision-making should be guided by clear protocols that incorporate real-time monitoring data, with regular updates to fault stability models as new information becomes available.

Our analysis of the TM field highlights a fundamental challenge in geothermal energy development: in fault-controlled systems, the same structural features that provide the necessary permeability for viable geothermal production are also the most susceptible to reactivation during operations. This creates complex trade-offs between renewable energy development and seismic hazard management that extend beyond technical considerations. Experiences from established geothermal fields worldwide illustrate varying approaches to managing seismicity. At The Geysers in California, the local community has generally accepted frequent small-magnitude events as part of long-term geothermal operations (McComas et al., 2016), while the Basel EGS project in Switzerland was terminated following public concern over induced seismic events (Renoth et al., 2023).

In tectonically active regions, operational strategies necessarily differ from stable continental settings. Iceland's geothermal operations demonstrate successful coexistence with seismicity through continuous monitoring and injection management (Juncu et al., 2020). These examples suggest that successful geothermal development in active rift segments such as Tulu Moye does not require the prevention of all induced seismicity, but rather the establishment of acceptable thresholds based on local geological and social contexts.

4.3. Limitations and Future Research Directions

Our static fault stability analysis provides essential baseline characterization but has inherent limitations that should be acknowledged. Our approach does not account for: (a) poroelastic stress changes during production and injection cycles, which can alter the stress field over distances exceeding the immediate injection zone (Segall & Fitzgerald, 1998); (b) thermoelastic effects from temperature variations, which become significant in high-temperature systems (Jeanne et al., 2014); (c) dynamic stress transfer from induced seismicity, which can trigger cascading failures on nearby faults (Catalli et al., 2016); and (d) transient pressure diffusion, which controls the temporal evolution of induced seismicity (Shapiro, 2015).

Two further simplifications warrant acknowledgment. First, the vertical stress calculation relies on a constant bulk density (2,500–2,800 kg/m^3), which may not capture local variations within the shallow clay cap and hydrothermal alteration zones; density deviations of this kind could modify σ_V by up to ~10%–15% locally. Second, hydrostatic pore fluid pressure is adopted as a baseline, whereas effective normal stresses in active geothermal reservoirs are sometimes considerably lower, potentially approaching 1 MPa at reservoir depth (e.g., Fournier, 1991). Both sources of uncertainty are, however, explicitly propagated through the Monte Carlo framework (Section 2.4), and the resulting distributions of fracture susceptibility (Figure 9b) reflect the full range of plausible conditions rather than a single deterministic estimate.

Despite these limitations, static analysis remains valuable for initial development planning. Our identification of critically stressed fault segments provides crucial input for: (a) optimising well trajectories to avoid high-risk structures, (b) designing monitoring networks focused on potentially active faults, and (c) establishing pre-

production baseline conditions. As operations commence at Tulu Moye, this static framework should evolve into coupled THMC models incorporating production data, temperature measurements, and observed seismicity patterns. The transition from static to dynamic modelling represents a natural progression in geothermal field management, as demonstrated in mature fields such as The Geysers and Larderello, where decades of operational data now inform sophisticated coupled models (Rutqvist et al., 2013).

A further limitation of the present analysis is the assumption of a laterally uniform and depth-averaged stress field. Stress orientation and magnitude are well-documented to vary with depth and laterally, particularly in geothermally active rift settings where local stress perturbations, such as magmatic intrusions and hydrothermal convection, introduce significant mechanical heterogeneity (Zoback, 2007). Should stress magnitudes or orientations change substantially with depth, the fault stability results presented here would require recalibration. We note, however, that the structural geometry underpinning our analysis is independently supported at reservoir depths by microseismic clustering and gravity data (Section 2.1; Greenfield et al., 2019b; Hochstein et al., 2017; Hilemichaeil et al., 2024; Nigussie et al., 2023), which lend confidence to the fault orientations used in the stability calculations. The static framework employed is most sensitive to changes in $\sigma 3$ magnitude and pore fluid pressure (Section 3.4), and lateral stress rotations exceeding $\sim 15°$ would meaningfully alter slip tendency predictions for obliquely oriented fault segments. Resolving such variations would require dedicated borehole-based measurements—hydraulic fracturing tests or wellbore breakout analysis—which are currently unavailable at Tulu Moye but represent a clear priority for future site characterization as the project advances.

5. Conclusions

The Tulu Moye geothermal field exemplifies the challenges of developing geothermal resources in actively deforming rift settings. Our study demonstrates that many faults in the region are critically stressed and close to reactivation under existing stress conditions. Integration of stress inversion from focal mechanisms with probabilistic fault stability analysis reveals that even modest increases in pore pressure (3–5 MPa) from fluid injection could trigger fault slip and potentially induce seismicity. Assessing risks governed by transient interactions among injection, heat extraction and stress redistribution will require coupled THM modeling beyond the present work.

Through detailed fault mapping, stress inversion, and Monte Carlo simulations, we identified pore fluid pressure as the dominant control on fault stability, accounting for 45% of the variability in stability predictions. This is particularly significant given the active hydrothermal system and planned geothermal operations. Our findings highlight the critical role of fault orientation relative to the current stress field, with the majority of mapped faults showing high slip tendency (>0.6) and thus being susceptible to reactivation. These results establish pre-production baseline conditions against which future operational changes can be assessed.

This study provides a framework for assessing fault stability in geothermal systems within tectonically active regions. The combined application of deterministic and probabilistic approaches offers a robust methodology for initial hazard assessment and quantifying uncertainties. While comprehensive risk management will ultimately require coupled THMC modeling as the field develops, successful development of such geothermal resources requires careful pressure management and comprehensive monitoring systems that can track both seismic activity and pore pressure changes in real-time. Our analysis provides the necessary baseline for designing these monitoring systems and establishing initial operational protocols, particularly critical in regions like the Main Ethiopian Rift where geothermal systems are heavily fault-controlled and tectonic activity is ongoing.

Conflict of Interest

The authors declare no conflicts of interest relevant to this study.

Availability Statement

(i) FracPaQ software for fault segment map and fault segment attributes (Healy, 2025a).
(ii) FracTend software for Slip Tendency, Dilation Tendency, Fault Susceptibility stereoplots and Mohr's Circles (Healy, 2025b).

(iii) Probability of fault slip (pfs) for Response Surface Methodology and Monte Carlo simulation applied to the calculation of probability for slip and dilation tendency (Healy, 2022).
(iv) Seismic Event Catalog for the Tulu Moye Geothermal Field, Ethiopia (2016–2017) (Rizzo et al., 2025).

All software used in this work are open source and are available from the following source:

Acknowledgments
The authors thank the Editor Whitney Behr and two anonymous reviewers whose constructive comments greatly improved the manuscript. This research was funded by the European Union-FESR FSE PON Ricerca e Innovazione 2014–2020 DM 1062/2021. R.E.R., D.K., and P.V. thank Reykjavik Geothermal as an industrial partner during the project. A.M. was funded by the German Research Foundation (DFG)—Grant 537025018. D. K. was partially supported through NERC Grant UKRI1277. Open access publishing facilitated by Universita degli Studi di Firenze, as part of the Wiley - CRUI-CARE agreement.

References

Agostini, A., Bonini, M., Corti, G., Sani, F., & Manetti, P. (2011). Distribution of quaternary deformation in the central Main Ethiopian Rift, East Africa. *Tectonics*, *30*(4). https://doi.org/10.1029/2010tc002833

Barton, C. A., Zoback, M. D., & Moos, D. (1995). Fluid flow along potentially active faults in crystalline rock. *Geology*, *23*(8), 683–686. https://doi.org/10.1130/0091-7613(1995)023<0683:ffapaf>2.3.co;2

Beaucé, E., Van Der Hilst, R. D., & Campillo, M. (2022). An iterative linear method with variable shear stress magnitudes for estimating the stress tensor from earthquake focal mechanism data: Method and examples. *Bulletin of the Seismological Society of America*, *112*(3), 1224–1239. https://doi.org/10.1785/0120210319

Biggs, J., Bastow, I. D., Keir, D., & Lewi, E. (2011). Pulses of deformation reveal frequently recurring shallow magmatic activity beneath the Main Ethiopian Rift. *Geochemistry, Geophysics, Geosystems*, *12*(9). https://doi.org/10.1029/2011gc003662

Biot, M. A. (1941). General theory of three-dimensional consolidation. *Journal of Applied Physics*, *12*(2), 155–164. https://doi.org/10.1063/1.1712886

Bonini, M., Boccaletti, M., Mazzuoli, R., & Trua, T. (1999). Pliocene, quaternary volcanism and faulting in the northern main Ethiopian Rift (with two geological maps at scale 1:50000). *Acta Vulcanologica*, *11*, 83–97.

Catalli, F., Rinaldi, A. P., Gischig, V., Nespoli, M., & Wiemer, S. (2016). The importance of earthquake interaction for injection-induced seismicity: Retrospective modelling of the Basel Enhanced Geothermal System. *Geophysical Research Letters*, *43*(10), 4992–4999. https://doi.org/10.1002/2016gl068932

Corti, G., Sani, F., Florio, A. A., Greenfield, T., Keir, D., Erbello, A., et al. (2020). Tectonics of the Asela-Langano margin, Main Ethiopian Rift (East Africa). *Tectonics*, *39*(8), e2020TC006075. https://doi.org/10.1029/2020tc006075

Detournay, E., & Cheng, A. H. D. (1993). Fundamentals of poroelasticity. In *Analysis and design methods* (pp. 113–171). Pergamon.

Evans, K. F., Zappone, A., Kraft, T., Deichmann, N., & Moia, F. (2012). A survey of the induced seismic responses to fluid injection in geothermal and CO2 reservoirs in Europe. *Geothermics*, *41*, 30–54. https://doi.org/10.1016/j.geothermics.2011.08.002

Ferrill, D. A., Smart, K. J., & Morris, A. P. (2020). Fault failure modes, deformation mechanisms, dilation tendency, slip tendency, and conduits v. seals.

Fournier, R. O. (1991). The transition from hydrostatic to greater than hydrostatic fluid pressure in presently active continental hydrothermal systems in crystalline rock. *Geophysical Research Letters*, *18*(5), 955–958.

Greenfield, T., Keir, D., Kendall, J. M., & Ayele, A. (2019a). Seismicity of the Bora-Tullu Moye volcanic field, 2016–2017. *Geochemistry, Geophysics, Geosystems*, *20*(2), 548–570. https://doi.org/10.1029/2018gc007648

Greenfield, T., Keir, D., Kendall, J. M., & Ayele, A. (2019b). Low-frequency earthquakes beneath Tulu Moye volcano, Ethiopia, reveal fluid pulses from shallow magma chamber. *Earth and Planetary Science Letters*, *526*, 115782. https://doi.org/10.1016/j.epsl.2019.115782

Grigoli, F., Cesca, S., Rinaldi, A. P., Manconi, A., López-Comino, J. A., Clinton, J. F., et al. (2018). The November 2017 Mw 5.5 Pohang earthquake: A possible case of induced seismicity in South Korea. *Science*, *360*(6392), eaat2010-1006. https://doi.org/10.1126/science.aat2010

Guo, H., Thurber, C., Warren, I., Heath, B. A., Folsom, M., Sone, H., et al. (2023). Enhanced microseismicity during production pumping cessation at the San Emidio geothermal field (Nevada, USA) in December 2016. *Journal of Geophysical Research: Solid Earth*, *128*(11), e2023JB027008. https://doi.org/10.1029/2023jb027008

Guðbrandsson, S., Eysteinsson, H., Mamo, T., Cervantes, C., & Gíslason, G. (2020). Geology and conceptual model of the Tulu Moye geothermal project, Oromia, Ethiopia. In *Proceedings world geothermal congress 2020* (p. 8). Reykjavik.

Healy, D. (2022). pfs: Version 0.9 [Code and Dataset]. *Zenodo*. https://doi.org/10.5281/zenodo.5825274

Healy, D. (2025a). FracPaQ (FracPaQ-V-2.6.1) [Software]. *Zenodo*. https://doi.org/10.5281/zenodo.17254351

Healy, D. (2025b). FracTend (FracTend-V1.0) [Software]. *Zenodo*. https://doi.org/10.5281/zenodo.17254343

Healy, D., & Hicks, S. P. (2022). De-risking the energy transition by quantifying the uncertainties in fault stability. *Solid Earth*, *13*(1), 15–39. https://doi.org/10.5194/se-13-15-2022

Healy, D., Rizzo, R. E., Cornwell, D. G., Farrell, N. J., Watkins, H., Timms, N. E., et al. (2017). FracPaQ: A MATLAB™ toolbox for the quantification of fracture patterns. *Journal of Structural Geology*, *95*, 1–16. https://doi.org/10.1016/j.jsg.2016.12.003

Hennings, P. H., Nicot, J. P., Gao, R. S., DeShon, H. R., Lund Snee, J. E., Morris, A. P., et al. (2021). Pore pressure threshold and fault slip potential for induced earthquakes in the Dallas-fort worth area of North Central Texas. *Geophysical Research Letters*, *48*(15), e2021GL093564. https://doi.org/10.1029/2021gl093564

Hicks, S. P., Goes, S., Whittaker, A. C., & Stafford, P. J. (2021). Multivariate statistical appraisal of regional susceptibility to induced seismicity: Application to the Permian Basin, SW United States. *Journal of Geophysical Research: Solid Earth*, *126*(12), e2021JB022768. https://doi.org/10.1029/2021jb022768

Hilemichaeil, S., Haile, T., & Yirgu, G. (2024). Integrated geophysical methods to constrain subsurface structures of Tulu Moye-Bora-Berecha axial volcanic complex, main Ethiopian rift: Implications for geothermal resources. *Heliyon*, *10*(7).

Hincks, T., Aspinall, W., Cooke, R., & Gernon, T. (2018). Oklahoma's induced seismicity strongly linked to wastewater injection depth. *Science*, *359*(6381), 1251–1255. https://doi.org/10.1126/science.aap7911

Hochstein, M. P., Oluma, B., & Hole, H. (2017). Early exploration of the Aluto geothermal field, Ethiopia (history of discovery well LA-3). *Geothermics*, *66*, 73–84. https://doi.org/10.1016/j.geothermics.2016.11.010

Hopp, C., Sewell, S., Mroczek, S., Savage, M., & Townend, J. (2019). Seismic response to injection well stimulation in a high-temperature, high-permeability reservoir. *Geochemistry, Geophysics, Geosystems*, *20*(6), 2848–2871. https://doi.org/10.1029/2019gc008243

Hutchison, W., Mather, T. A., Pyle, D. M., Biggs, J., & Yirgu, G. (2015). Structural controls on fluid pathways in an active rift system: A case study of the Aluto volcanic complex. *Geosphere*, *11*(3), 542–562. https://doi.org/10.1130/ges01119.1

International Energy Agency-IEA. (2024). *The future of geothermal energy*. IEA. Retrieved from https://www.iea.org/reports/the-future-of-geothermal-energy

Jaeger, J. C., Cook, N. G. W., & Zimmerman, R. W. (2007). Fundamental of rock mechanics (pp. 9–197).

Jeanne, P., Rutqvist, J., Vasco, D., Garcia, J., Dobson, P. F., Walters, M., et al. (2014). The impacts of mechanical stress transfers caused by hydromechanical and thermal processes on fault stability during hydraulic stimulation in a deep geothermal reservoir. *International Journal of Rock Mechanics and Mining Sciences*, *72*, 149–163. https://doi.org/10.1016/j.ijrmms.2014.09.005

JPL NASA. (2020). NASADEM Slope and Curvature Global 1 arc second V001 [Dataset]. *NASA EOSDIS Land Processes Distributed Active Archive Center*. https://doi.org/10.5067/MEaSUREs/NASADEM/NASADEM_SC.001

Juncu, D., Árnadóttir, T., Geirsson, H., Guðmundsson, G. B., Lund, B., Gunnarsson, G., et al. (2020). Injection-induced surface deformation and seismicity at the Hellisheiði geothermal field, Iceland. *Journal of Geophysical Research: Solid Earth*, *125*(8), e2019JB018643. https://doi.org/10.1016/j.jvolgeores.2018.03.019

Kebede, B. A., Pagli, C., Sigmundsson, F., Keir, D., La Rosa, A., & Guðbrandsson, S. (2023). Constraints on ground deformation processes at the Tulu Moye volcanic complex, Main Ethiopian Rift. *Journal of Volcanology and Geothermal Research*, *438*, 107810. https://doi.org/10.1016/j.jvolgeores.2023.107810

Keir, D., Stuart, G. W., Jackson, A., & Ayele, A. (2006). Local earthquake magnitude scale and seismicity rate for the Ethiopian rift. *Bulletin of the Seismological Society of America*, *96*(6), 2221–2230. https://doi.org/10.1785/0120060051

Kim, K. H., Ree, J. H., Kim, Y., Kim, S., Kang, S. Y., & Seo, W. (2018). Assessing whether the 2017 M w 5.4 Pohang earthquake in South Korea was an induced event. *science*, *360*(6392), 1007–1009. https://doi.org/10.1126/science.aat6081

Kivi, I. R., Pujades, E., Rutqvist, J., & Vilarrasa, V. (2022). Cooling-induced reactivation of distant faults during long-term geothermal energy production in hot sedimentary aquifers. *Scientific Reports*, *12*(1), 2065. https://doi.org/10.1038/s41598-022-06067-0

Laó-Dávila, D. A., Al-Salmi, H. S., Abdelsalam, M. G., & Atekwana, E. A. (2015). Hierarchical segmentation of the Malawi Rift: The influence of inherited lithospheric heterogeneity and kinematics in the evolution of continental rifts. *Tectonics*, *34*(12), 2399–2417. https://doi.org/10.1002/2015tc003953

Lee, K. K., Ellsworth, W. L., Giardini, D., Townend, J., Ge, S., Shimamoto, T., et al. (2019). Managing injection-induced seismic risks. *Science*, *364*(6442), 730–732. https://doi.org/10.1126/science.aax1878

Lisle, R. J., & Srivastava, D. C. (2004). Test of the frictional reactivation theory for faults and validity of fault-slip analysis. *Geology*, *32*(7), 569–572. https://doi.org/10.1130/g20408.1

Liu, S., Xu, L., & Talwani, P. (2011). Reservoir induced seismicity in the Dajangkou Reservoir: A quantitative analysis. *Geophysical Journal International*, *185*, 514–526.

Lund, B., & Slunga, R. (1999). Stress tensor inversion using detailed microearthquake information and stability constraints: Application to Olfus in southwest Iceland. *Journal of Geophysical Research*, *104*(B7), 14.947–14.964. https://doi.org/10.1029/1999jb900111

Majer, E. L., Baria, R., Stark, M., Oates, S., Bommer, J., Smith, B., & Asanuma, H. (2007). Induced seismicity associated with enhanced geothermal systems. *Geothermics*, *36*(3), 185–222. https://doi.org/10.1016/j.geothermics.2007.03.003

McComas, K. A., Lu, H., Keranen, K. M., Furtney, M. A., & Song, H. (2016). Public perceptions and acceptance of induced earthquakes related to energy development. *Energy Policy*, *99*, 27–32. https://doi.org/10.1016/j.enpol.2016.09.026

Michael, A. J. (1984). Determination of stress from slip data: Faults and folds. *Journal of Geophysical Research*, *89*(B13), 11.517–11.526. https://doi.org/10.1029/jb089ib13p11517

Michael, A. J. (1987). Use of focal mechanisms to determine stress: A control study. *Journal of Geophysical Research*, *92*(B1), 357–368. https://doi.org/10.1029/jb092ib01p00357

Moein, M. J., Langenbruch, C., Schultz, R., Grigoli, F., Ellsworth, W. L., Wang, R., et al. (2023). The physical mechanisms of induced earthquakes. *Nature Reviews Earth and Environment*, *4*(12), 847–863. https://doi.org/10.1038/s43017-023-00497-8

Morris, A., Ferrill, D. A., & Henderson, D. B. (1996). Slip-tendency analysis and fault reactivation. *Geology*, *24*(3), 275–278. https://doi.org/10.1130/0091-7613(1996)024<0275:staafr>2.3.co;2

Muluneh, A. A., Kidane, T., Corti, G., & Keir, D. (2018). Constraints on fault and crustal strength of the Main Ethiopian Rift from formal inversion of earthquake focal mechanism data. *Tectonophysics*, *731*, 172–180. https://doi.org/10.1016/j.tecto.2018.03.010

NASA Shuttle Radar Topography Mission (SRTM) (2013). *Shuttle Radar Topography Mission (SRTM) global*. Distributed by OpenTopography. https://doi.org/10.5069/G9445JDF

Nigussie, W., Alemu, A., Mickus, K., Keir, D., Demissie, Z., Muhabaw, Y., et al. (2023). Subsurface structural control of geothermal resources in a magmatic rift: Gravity and magnetic study of the Tulu Moye geothermal prospect, Main Ethiopian Rift. *Frontiers in Earth Science*, *11*, 1181533. https://doi.org/10.3389/feart.2023.1181533

Raesenberg, P. A., & Simpson, R. W. (1992). Response of regional seismicity to the static stress change produced in the Loma Prieta earthquake. *Science*, *255*, 1687–1690.

Renoth, R., Buchner, E., Schmieder, M., Keim, M., Plechaty, M., & Drews, M. (2023). Social acceptance of geothermal technology on a global view: A systematic review. *Energy Sustainability and Society*, *13*(1), 49. https://doi.org/10.1186/s13705-023-00432-1

Rizzo, R. E., Muluneh, A. A., & Keir, D. (2025). Seismic event catalogue for the Tullu Moye geothermal field, Ethiopia (2016-2017) [Dataset]. *Zenodo*. https://doi.org/10.5281/zenodo.14906812

Rodriguez, E., Morris, C. S., & Belz, J. E. (2006). A global assessment of the SRTM performance. *Photogrammetric Engineering and Remote Sensing*, *72*(3), 249–260. https://doi.org/10.14358/pers.72.3.249

Rutqvist, J., Dobson, P. F., Garcia, J., Hartline, C., Jeanne, P., Oldenburg, C. M., et al. (2013). The northwest Geysers EGS demonstration project, California: Pre-stimulation modeling and interpretation of the stimulation. *Mathematical Geosciences*, *47*(1), 3–29. https://doi.org/10.1007/s11004-013-9493-y

Samrock, F., Grayver, A. V., Eysteinsson, H., & Saar, M. O. (2018). Magnetotelluric image of transcrustal magmatic system beneath the Tulu Moye geothermal prospect in the Ethiopian Rift. *Geophysical Research Letters*, *45*(23), 12–847. https://doi.org/10.1029/2018gl080333

Schwab, D. R., Bidgoli, T. S., & Taylor, M. H. (2017). Characterizing the potential for injection-induced fault reactivation through subsurface structural mapping and stress field analysis, Wellington Field, Sumner County, Kansas. *Journal of Geophysical Research: Solid Earth*, *122*(12), 10–132. https://doi.org/10.1002/2017jb014071

Segall, P., & Fitzgerald, S. D. (1998). A note on induced stress changes in hydrocarbon and geothermal reservoirs. *Tectonophysics*, *289*(1–3), 117–128. https://doi.org/10.1016/s0040-1951(97)00311-9

Shapiro, S. A. (2015). *Fluid-induced seismicity*. Cambridge University Press.

Stein, R. S. (1999). Tidal triggering caught in act. *Nature*, *402*(6762), 605–609. https://doi.org/10.1038/45144

Streit, J. E., & Hillis, R. R. (2004). Estimating fault stability and sustainable fluid pressures for underground storage of CO_2 in porous rock. *Energy*, *29*(9–10), 1445–1456. https://doi.org/10.1016/j.energy.2004.03.078

Vavryčuk, V. (2014). Iterative joint inversion for stress and fault orientations from focal mechanisms. *Geophysical Journal International*, *199*(1), 69–77. https://doi.org/10.1093/gji/ggu224

Wedmore, L. N., Turner, T., Biggs, J., Williams, J. N., Sichingabula, H. M., Kabumbu, C., & Banda, K. (2022). The Luangwa Rift Active Fault Database and fault reactivation along the southwestern branch of the East African Rift. *Solid Earth*, *13*(11), 1731–1753. https://doi.org/10.5194/se-13-1731-2022

Zang, A., Oye, V., Jousset, P., Deichmann, N., Gritto, R., McGarr, A., et al. (2014). Analysis of induced seismicity in geothermal reservoirs–An overview. *Geothermics*, *52*, 6–21. https://doi.org/10.1016/j.geothermics.2014.06.005

Zbinden, D., Rinaldi, A. P., Diehl, T., & Wiemer, S. (2020). Potential influence of overpressurized gas on the induced seismicity in the St. Gallen deep geothermal project (Switzerland). *Solid Earth*, *11*(3), 909–933. https://doi.org/10.5194/se-11-909-2020

Zoback, M. D. (2007). *Reservoir geomechanics*. Cambridge University Press.

Zoback, M. D., Barton, C. A., Brudy, M., Castillo, D. A., Finkbeiner, T., Grollimund, B. R., et al. (2003). Determination of stress orientation and magnitude in deep wells. *International Journal of Rock Mechanics and Mining Sciences*, *40*(7–8), 1049–1076. https://doi.org/10.1016/j.ijrmms.2003.07.001